




Article

Application of Commercial Surface Pretreatments on the Formation of Cerium Conversion Coating (CeCC) over High-Strength Aluminum Alloys 2024-T3 and 7075-T6

Juan Jesús Alba-Galvín ¹, Leandro González-Rovira ^{1,2,*}, Francisco Javier Botana ^{1,2}, Maria Lekka ^{3,4},
Francesco Andreatta ³, Lorenzo Fedrizzi ³ and Manuel Bethencourt ⁵

¹ Department of Materials Science, Metallurgical Engineering and Inorganic Chemistry, Engineering School, Universidad de Cádiz, 11519 Puerto Real, Cádiz, Spain; juanjesus.alba@uca.es (J.J.A.-G.); javier.botana@uca.es (F.J.B.)

² IMEYMAT: Institute of Research on Electron Microscopy and Materials, Universidad de Cádiz, 11510 Puerto Real, Cádiz, Spain

³ Polytechnic Department of Engineering and Architecture, University of Udine, Via del Cotonificio 108, 33100 Udine, Italy; mlekk@cidetec.es (M.L.); francesco.andreatta@uniud.it (F.A.); lorenzo.fedrizzi@uniud.it (L.F.)

⁴ CIDETEC, Parque Científico y Tecnológico de Gipuzkoa, Pº Miramón, 191, 20014 Donostia-San Sebastián, Guipúzcoa, Spain

⁵ Department of Materials Science, Metallurgical Engineering and Inorganic Chemistry, Faculty of Marine and Environmental Sciences, Universidad de Cádiz, International Campus of Excellence of the Sea (CEI-MAR), 11510 Puerto Real, Cádiz, Spain; manuel.bethencourt@uca.es

* Correspondence: leandro.gonzalez@uca.es; Tel.: +34-956-016-762



Citation: Alba-Galvín, J.J.; González-Rovira, L.; Botana, F.J.; Lekka, M.; Andreatta, F.; Fedrizzi, L.; Bethencourt, M. Application of Commercial Surface Pretreatments on the Formation of Cerium Conversion Coating (CeCC) over High-Strength Aluminum Alloys 2024-T3 and 7075-T6. *Metals* **2021**, *11*, 930. <https://doi.org/10.3390/met11060930>

Academic Editor: Koh-ichi Sugimoto

Received: 10 May 2021

Accepted: 3 June 2021

Published: 7 June 2021

Publisher's Note: MDPI stays neutral with regard to jurisdictional claims in published maps and institutional affiliations.



Copyright: © 2021 by the authors. Licensee MDPI, Basel, Switzerland. This article is an open access article distributed under the terms and conditions of the Creative Commons Attribution (CC BY) license (<https://creativecommons.org/licenses/by/4.0/>).

Abstract: The selection of appropriate surface pretreatments is one of the pending issues for the industrial application of cerium-based chemical conversion coatings (CeCC) as an alternative for toxic chromate conversion coating (CrCC). A two-step surface pretreatment based on commercial products has been successfully used here to obtain CeCC on AA2024-T3 and AA7075-T6. Specimens processed for 1 to 15 min in solutions containing CeCl₃ and H₂O₂ have been studied by scanning electron microscopy coupled with energy-dispersive X-ray analysis (SEM-EDX), glow discharge optical emission spectroscopy (GDOES), potentiodynamic linear polarization (LP), electrochemical impedance spectroscopy (EIS), and neutral salt spray (NSS) tests. SEM-EDX showed that CeCC was firstly observed as deposits, followed by a general coverage of the surface with the formation of cracks where the coating was getting thicker. GDOES confirmed an increase of the CeCC thickness as the deposition proceed, the formation of CeCC over 7075 being faster than over 2024. There was a Ce-rich layer in both alloys and an aluminum oxide/hydroxide layer on 7075 between the upper Ce-rich layer and the aluminum matrix. According to LP and EIS, CeCC in all samples offered cathodic protection and comparable degradation in chloride-containing media. Finally, the NSS test corroborated the anti-corrosion properties of the CeCC obtained after the commercial pretreatments employed.

Keywords: aluminum; alloy phases; corrosion; surface pretreatments; CeCC

1. Introduction

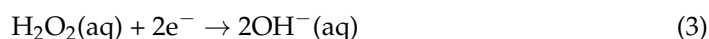
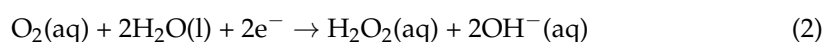
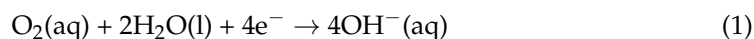
High-strength aluminum alloys are the primary structural material for aircrafts thanks to their good workability and high specific strength. Among them, 2024 of 2000 (Al-Cu-Mg) series and 7075 of 7000 (Al-Zn-Mg) series are the most common alloys used. However, the presence of alloying elements reduces the corrosion resistance of these alloys due to galvanic coupling between intermetallic particles (IMPs) and the aluminum matrix [1–3]. As a consequence, 2024 and 7075 alloys usually require protective surface treatments.

There are many surface treatments, such as anodizing, chemical conversion coating, or organic coatings. Many of them have traditionally employed chromates for both improving

the corrosion resistance and enhancing paint chemical adhesion [4–8]. Chromates are used as inhibitors in closed systems and paints, in Cr-based chemical conversion coatings (CrCC), and in anodizing and sealing baths [9–11]. Among these applications, CrCC is especially successful since chromium species are present in two oxidation states: Cr(III) and Cr(VI). On one hand, the chromium Cr(III) species offer a barrier protective effect in the form of Cr(III) oxide (Cr_2O_3). On the other hand, the reduction of Cr(VI) species at eventual coating defects to form the passivating Cr_2O_3 coating provides self-healing behavior.

However, hexavalent chromium presents toxicity and carcinogenic properties, and is prohibited by several regulations (REACH EU Regulation EC No. 1907/2006 or OSHA final standard of 2006). Great efforts have been made in order to look for alternatives to CrCC [12]. The great number of possibilities includes conversion coatings based on trivalent chromium [13], rare earths chemical conversion coatings [14,15], Zr/Ti-based chemical conversion coatings [16], sol-gel coatings [17], and smart coatings providing self-healing protection [12,18,19]. However, none of these options has achieved a true industrial application capable of replacing CrCC and the scientific community continues to search for an alternative. Still today, one of the most promising candidates for chromate conversion coating replacement is cerium-based chemical conversion coatings (CeCC) [11,14,20–22].

The formation of CeCC coatings involves redox and precipitation reactions which produce the conversion from soluble cerium salt to insoluble cerium oxide and/or hydroxide [23–26]. In brief, oxygen is reduced to OH^- over areas or IMPs which are electrochemically more noble than the surrounding aluminum matrix, Equations (1) and (2). Sometimes, H_2O_2 is added to the solution as an oxidant (catalyst) in order to promote the production of OH^- ions, Equation (3). The corresponding anodic reaction is the oxidation of the aluminum matrix, Equation (4). Afterwards, the local increase of pH due to the production of OH^- ions close to the cathodic sites provokes the precipitation of Ce(III) oxide and/or hydroxide. In addition, Ce(III) can oxidize to Ce(IV) through different mechanisms, giving rise to different proportions of Ce(III)/Ce(IV) in the coatings. As a result, the CeCC process yields a coating formed by Al_2O_3 and cerium oxide and/or hydroxide with variable rates of Ce(III)/Ce(IV).



Although studied from the 1980s, there are still uncertainties in this technology that hinder its industrial application. One of the issues is the influence of surface pretreatment on the morphology and chemistry of the alloy surface, since they subsequently affect the deposition process and the properties of the CeCC coating. In effect, like most surface treatments, CeCC processes require pretreatments like cleaning or etching in order to degrease the surface, remove inorganic contamination, or eliminate the native oxide layer. Otherwise, cerium will generally not deposit on a non-pretreated surface, even on active alloys like 2024 and 7075 [14].

Currently, the effect of commercial solutions or laboratory-scale pretreatments remain not completely understood [27,28]. Moreover, some of the pretreatments employed in the literature would not be suitable in an industrial context. From an industrial point of view, it is desirable that the alternative to CrCC is compatible with the same pretreatments currently approved. Otherwise, the investments required to adapt the corrosion protective treatment must include the pretreatments as well. Thus, in a previous paper [29], the authors investigated the effect of a standard surface pretreatment for aluminum alloys in the aeronautical industry on the 2024-T3 surface and its subsequent influence in the formation of CeCC in solutions of CeCl_3 and H_2O_2 . The standard pretreatment comprises the immersion of the parts in three consecutive chemical solutions: (a) Turco 6849: a silicate-containing alkaline degreaser, (b) Turco 4215 NC-LT: a free of chromate and silicate alkaline

etching, and (c) Turco Smut Go NC: an oxidizing acid pickling. The results showed that the cerium-based coating formed after the employment of only the chemical solutions (a) and (b) (Turco 6849 and Turco 4215 NC-LT) has better corrosion behavior than applying the whole chain.

The present paper is the continuation of this research line. Here, the applicability of the pretreatment previously selected is further studied for the formation of CeCC coatings on aluminum alloys 2024 and 7075. Specifically, the focus is put on the morphology, composition, and corrosion behavior of coatings formed during CeCC treatments from 1 to 15 min in solutions containing CeCl_3 and H_2O_2 with pH adjusted to 1.9. The morphology and composition of the coatings were studied by scanning electron microscopy coupled with energy-dispersive X-ray analysis (SEM-EDX) and glow discharge optical emission spectroscopy (GDOES). Meanwhile, potentiodynamic linear polarization (LP), electrochemical impedance spectroscopy (EIS), and neutral salt spray (NSS) tests were employed to analyze the corrosion properties.

2. Materials and Methods

Samples of the aluminum alloys 2024-T3 and 7075-T6 of 80 mm × 25 mm × 1 mm in size were employed. The composition of the alloys, certified by the metal manufacturer (Castle Metals France) in percentage by mass, is shown in Table 1.

Table 1. Chemical composition (wt. %) of aluminum alloys 2024-T3 and 7075-T6.

Alloy	Si	Fe	Cu	Mn	Mg	Cr	Zn	Ti	Ti + Zr	V	Al	Others
2024-T3	0.07	0.19	4.30	0.58	1.30	0.01	0.10	0.02	-	0.01	93.42	-
7075-T6	0.08	0.13	1.7	0.02	2.5	0.19	5.7	0.04	0.04	-	89.61	0.03

Before the pretreatments, specimens were rinsed with acetone in order to remove adhesive rests coming from a plastic protective film and ink residues. The pretreatments involved two consecutive steps: (i) 7 min stirring alkaline cleaning at 55 °C in 20 vol. % Turco 6849 (pH = 10.9) and (ii) 10 min stirring alkaline etching at 50 °C in 40 g/L Turco 4215 NC-LT (pH = 8.9).

Turco 6849 and 4215 NC-LT were supplied by Henkel Ibérica, S.A., (Barcelona, Spain). Between each step, the samples were rinsed and immersed for 3 min in deionized water with a pH of 5.6 and a resistivity of 15 M Ω . CeCC were deposited in aqueous solution containing 25 mM $\text{CeCl}_3 \cdot 7\text{H}_2\text{O}$ (Alfa Aesar, Karlsruhe, Germany) and 15 mL/L 30 vol. % H_2O_2 (Panreac Química S.L.U., Barcelona, Spain) at 50 °C for 1, 5, 10, and 15 min. The pH value was adjusted to 1.9 employing 1 M HCl. The samples coated with alloys 2024 and 7075 were labeled as 2-Ce-X and 7-Ce-X, respectively, with X = 1, 5, 10, and 15 min.

The surface morphology and composition of the samples were studied by scanning electron microscopy (SEM) employing a Zeiss EVO 40 (Carl Zeiss AG, Oberkochen, Germany) equipped with an EDX probe (Oxford Instruments, Abingdon, UK). Glow discharge optical emission spectroscopy (GDOES) depth profiles were recorded with a Horiba Jobin Yvon Rf-GD-profiler (Horiba Ltd., Kyoto, Japan). The instrument was equipped with a standard 4-mm-diameter anode, a polychromator with 28 acquiring channels, an Rf generator (13.6 MHz), and a Quantum XP software. Semi-quantitative composition profiles were obtained with a calibration procedure using certified reference materials in order to estimate film thickness and composition.

Potentiodynamic linear polarization (LP) and electrochemical impedance spectroscopy (EIS) measurements were conducted in three-electrode cells, making use of a PGSTAT302N potentiostat with frequency response analyzer (FRA) (Metrohm Autolab B.V., Utrecht, The Netherlands) controlled by the software NOVA 2.1.2. An Ag/AgCl 3M from Metrohm (0.207 V/SHE, 25 °C) was employed as the reference electrode. The counter electrode was made of platinized titanium mesh. The exposed surface of the working electrode was 1 cm². Before the LP, the open circuit potential (OCP) was measured for 30 min (this time was experimentally observed to reach potential stabilization). LPs were carried out in

3.5% NaCl from -0.05 V to 1 V vs. corrosion potential (E_{corr}) at a scan rate of 0.17 mV/s. Immersion tests in 0.5% NaCl were monitored with EIS during 24 h. The interval of the EIS measurements was between 10^{-2} – 10^{+5} Hz and the amplitude selected was 10 mV.

A neutral salt spray (NSS) test was performed to evaluate the corrosion resistance of the CeCC coating against bare 2024 and 7075 alloy. Samples of 100 mm \times 150 mm \times 1 mm were tested in the company Titania, Ensayos y Proyectos Industriales according to ISO 9227 [30] and ASTM B117-16 [31] in a chamber Ascott S2000is with 2000 L of capacity (Ascott analytical Equipment Ltd., Staffordshire, UK). The concentration of NaCl in the sprayed solution was 5 ± 1 w/w %, the temperature 35 ± 2 °C, and the pH = 6.5–7.2. The spraying rate was in the range 1–2 mL/h and the samples were placed at 15–30° to the horizontal.

3. Results and Discussion

3.1. Scanning Electron Microscopy (SEM-EDX)

Figure 1 shows SEM images of samples 2-Ce-1, 2-Ce-5, 2-Ce-10, and 2-Ce-15. EDX analysis included in Table 2 was performed in the areas marked in each image (Supplementary Materials contain original EDX spectra in Figure S1). Sample 2-Ce-1 showed the typical microstructure of the 2024 alloy described in previous works [3,29], where the most common coarse IMPs were Al(Cu,Mg) and Al-Cu-Mn-Fe-(Si). SEM-EDX did not capture the presence of the peaks corresponding to Ce. Therefore, the deposition, if any, is not detectable with this technique.

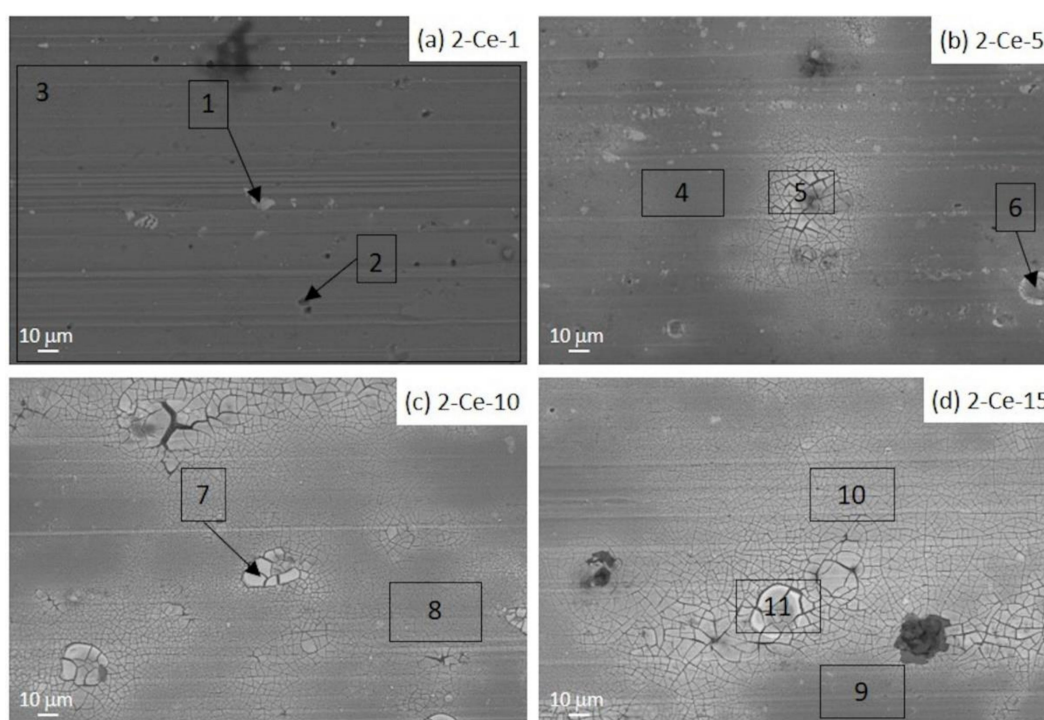


Figure 1. SEM images of 2024 samples: (a) 2-Ce-1, (b) 2-Ce-5, (c) 2-Ce-10, and (d) 2-Ce-15. EDX analyses were acquired in the points (arrows) or areas (square) marked.

Table 2. Semiquantitative EDX analyses (wt. %) in areas marked in Figure 1.

Area.	Al	Cu	Mg	O	Mn	Fe	C	Ce
1	52.33	20.81	1.28	2.81	3.59	6.36	12.64	-
2	88.65	4.85	2.01	4.48	-	-	-	-
3	81.19	3.64	1.62	2.95	0.49	-	10.11	-
4	68.57	3.90	1.18	14.21	-	-	5.50	6.64
5	38.48	3.73	-	27.22	-	-	5.75	24.81
6	44.38	15.04	1.05	24.70	1.28	1.26	-	9.41
7	0.89	-	-	26.71	-	-	-	72.40
8	55.05	3.31	1.16	22.58	-	-	-	17.90
9	74.22	3.50	1.39	14.01	-	-	-	6.78
10	41.95	3.32	0.60	26.87	-	-	6.53	20.73
11	31.80	3.18	-	29.78	-	-	5.60	29.68

Samples 2-Ce-5, 2-Ce-10, and 2-Ce-15 presented three types of morphologies associated with cerium layers: (a) deposits or copper islands typically formed on the intermetallic phases [24,29,32], (b) characteristic areas with cracked coating, and (c) uniform areas without cracking. However, there were still some areas in sample 2-Ce-5 where IMPs were appreciated. These were areas where either there was no deposition of the cerium layer or the layer was very thin. The EDX spectra of samples 2-Ce-5, 10, and 15 in Figure 1 did contain peaks of Ce, as displayed in Table 2. The other peaks are attributable to alloy elements: Al, Cu, Mg, Mn, and Fe. In addition, O could be found, mainly corresponding to aluminum oxide/hydroxide, and small amounts of C, assumed to come from organic contamination.

The number of Ce deposits and the area with cracked coating were observed to increase when the time of deposition also increased from 1 min up to 15 min. The microanalysis included in Table 2 for sample 2-Ce-15 indicates that the Ce and the O content increased as the analysis moved from the uniform zone (spectrum 9) to the area containing small cracks (spectrum 10) and then to that of wider cracks (spectrum 11). In contrast, the signals of Al, Cu, and Mg decreased in the order spectrum 9 > 10 > 11.

Similarly, spectrum 4 of sample 2-Ce-5, taken over a uniform area, had less Ce and more Al than spectrum 5, acquired on a cerium deposit. The same happened when comparing spectra 7 and 8 of sample 2-Ce-10. The uniform zone contained less Ce and more Al than the Ce deposit. Consequently, the increase in the number of Ce deposits and in the area with cracked coating with deposition time could reasonably be attributed to a thickening of the CeCC layer.

SEM images of samples 7-Ce-1, 7-Ce-5, 7-Ce-10, and 7-Ce-15 are included in Figure 2. The areas where EDX analyses included in Table 3 were performed are marked in each case (Supplementary Materials contain original EDX spectra in Figure S2). On this occasion, Ce deposits or copper islands were observed in the sample 7-Ce-1 and Ce was detected in both deposits spectra 2 and 3, and outside them, spectrum 1, although in a lower proportion in the latter. In certain areas of sample 7-Ce-1, IMPs of this alloy may be faintly observed in the SEM image. Contrariwise, there were only cerium deposits and coated areas with or without cracks in samples 7-Ce-5, 7-Ce-10, and 7-Ce-15. As described above for the coated samples of 2024, cracked areas increased their proportion with deposition time, so that in the 7-Ce-15 there were almost no crack-free zones. Semiquantitative EDX analyses obtained on deposits or areas with large cracks, spectra 5, 6, and 8, exhibited a higher quantity of Ce and less Al than areas with smaller cracks, spectra 4, 7, and 9.

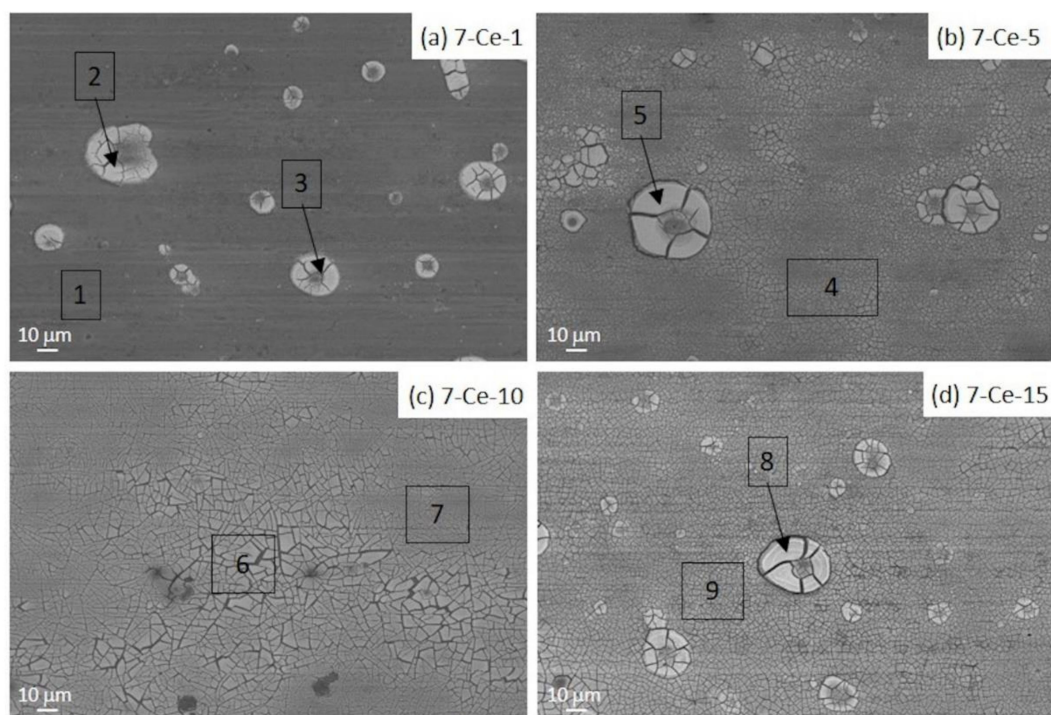


Figure 2. SEM images of 7075 samples: (a) 7-Ce-1, (b) 7-Ce-5, (c) 7-Ce-10, and (d) 7-Ce-15. EDX analyses were acquired in the points (arrows) or areas (square) marked.

Table 3. Semiquantitative EDX analyses (wt. %) in areas marked in Figure 2.

Area	Al	Cu	Mg	O	Zn	C	Ce
1	70.52	1.59	2.76	16.02	5.35	-	3.76
2	36.82	-	2.12	27.24	3.26	7.01	23.55
3	27.39	0.82	0.97	27.68	2.92	6.42	33.80
4	40.41	0.87	1.27	27.16	4.78	6.27	19.19
5	20.37	-	0.66	29.02	2.57	4.77	42.61
6	30.54	-	1.26	28.33	3.28	-	36.59
7	4.07	1.19	-	25.60	4.12	6.99	22.04
8	0.62	-	-	12.45	-	-	86.93
9	43.80	-	1.05	28.26	4.38	-	22.51

According to the literature [33], the formation of cracks is dependent on a number of factors such as type of cerium ions, hydrogen peroxide concentration, pH of the solution, and conversion time. It is also thought that cracks appear when the water evaporates during the drying process or even due to the vacuum inside the SEM microscope chamber. In any case, the coating with high thickness will be more susceptible to cracking. The coating morphologies found here were in good agreement with those described in the literature [14,15]. In [15], Al 2024-T3 and 7075-T7 alloys were grounded and polished prior to being employed to study Ce- and La-chloride conversion coatings. The influence of temperature, conversion time, and addition of hydrogen peroxide on the morphology, composition, and corrosion properties of the coatings were analyzed. When using 0.01 M CeCl_3 , 60 °C, and 0.13 M H_2O_2 , similar conversion conditions to those employed here, they detected the formation of cerium oxide or hydroxide proceeds preferentially at the IMPs and that cracks were observed when the deposition time was increased, which they also attributed to a greater thickness of the coating.

3.2. Glow Discharge Optical Emission Spectroscopy (GDOES)

The composition depth profiles of Ce, O, and Al expressed in wt.% obtained in CeCC deposited at the different times are included in Figures 3 and 4.

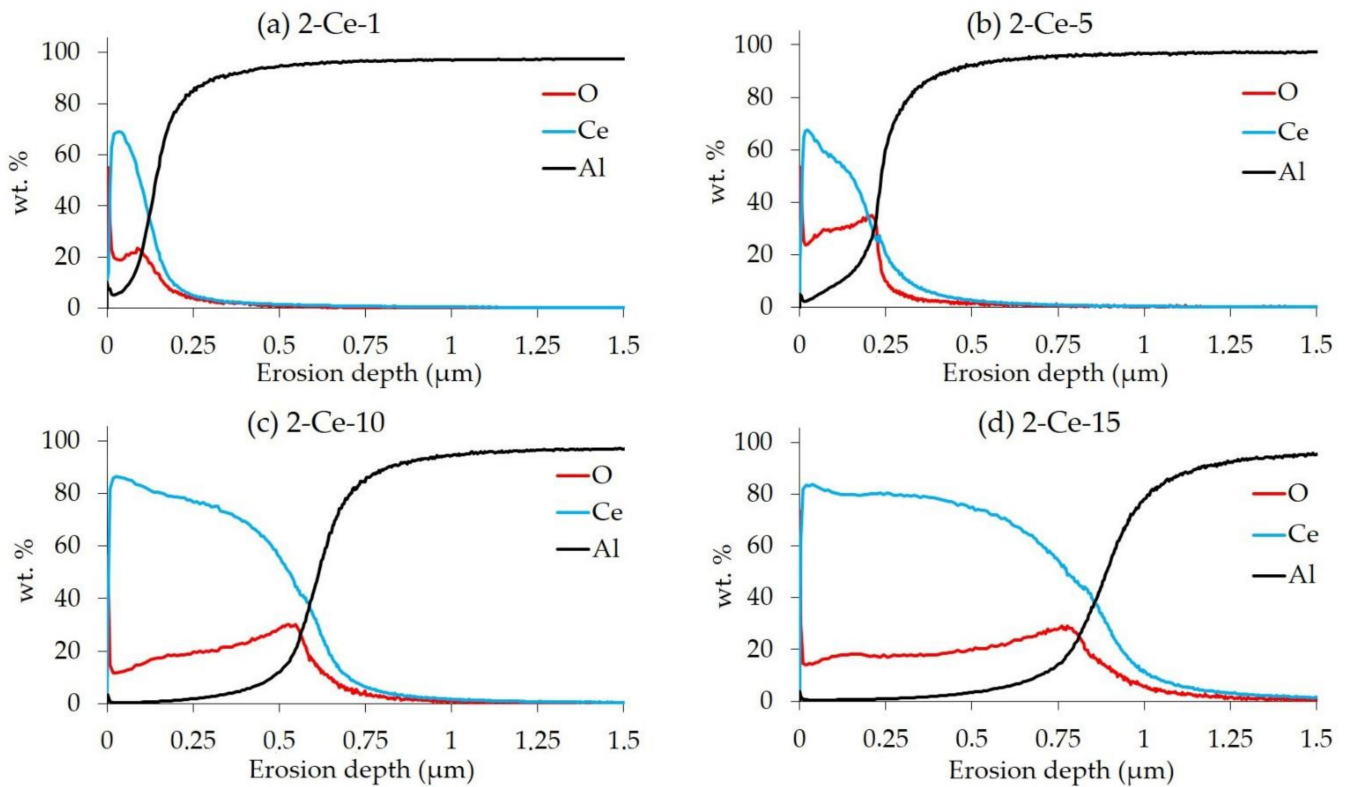


Figure 3. GDOES depth profiles of 2024 samples: (a) 2-Ce-1, (b) 2-Ce-5, (c) 2-Ce-10, and (d) 2-Ce-15.

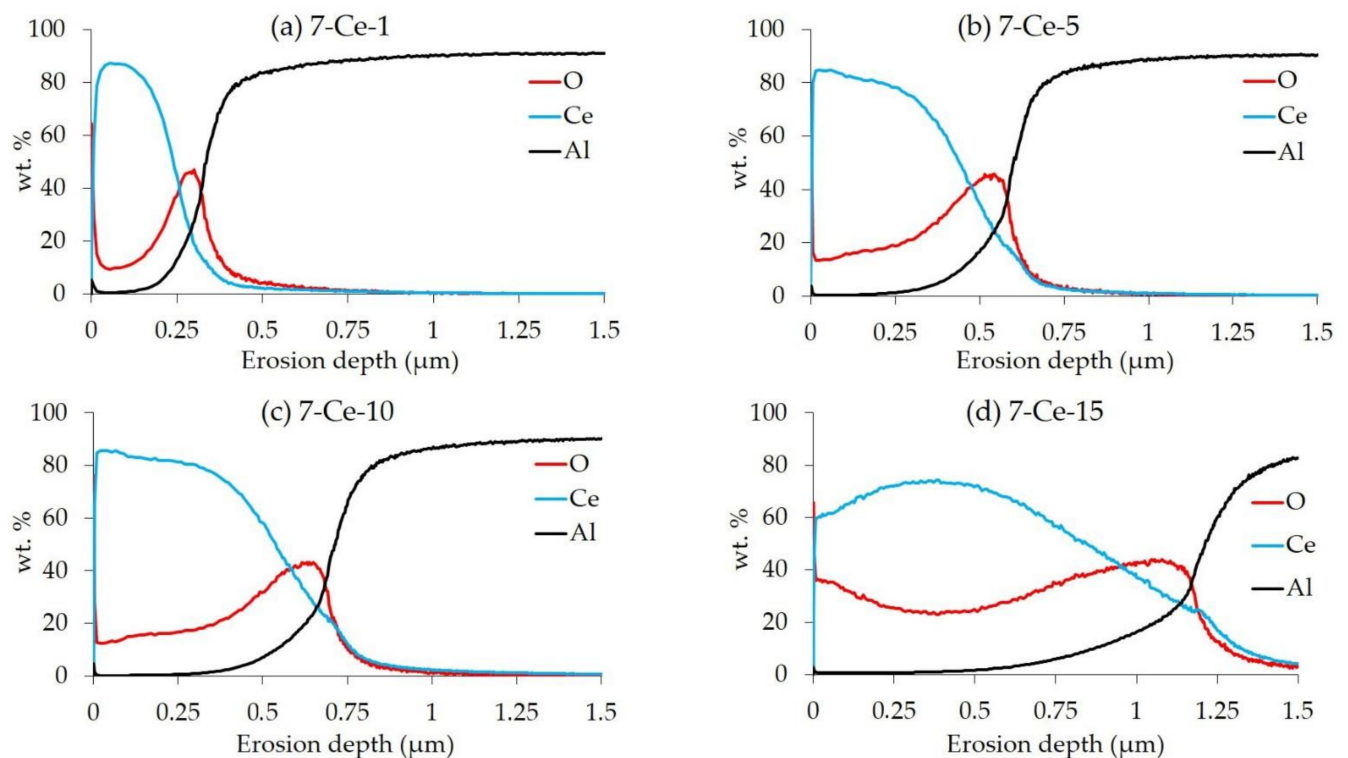


Figure 4. GDOES depth profiles of 7075 samples: (a) 7-Ce-1, (b) 7-Ce-5, (c) 7-Ce-10, and (d) 7-Ce-15.

Two sections could be distinguished in the profiles of alloy 2024. A first outer section (on the left side of all profiles in Figure 3) in which the main element was cerium, corresponding to the CeCC, and a second inner section (on the right side of all profiles in Figure 3) in which the main element was aluminum, corresponding to the alloy matrix. In the case of alloy 7075, three zones were observed in all profiles in Figure 4, the same two described for 2024 and a third one between them, in which the main element was oxygen. This intermediate section can be attributed to the existence of a layer of both aluminum oxides and hydroxides between the metal matrix and the CeCC [34–36]. The peak of the O signal close to the substrate was also visible for AA2024 although less evident than for AA7075. This trend of the O signal could be ascribed to a different structure of the conversion layer: higher amount of hydroxides near the surface and higher amount of oxides closer to the substrate. This interpretation does not mean that there is no aluminum oxide/hydroxide layer on the coating of alloy 2024. The aluminum oxide/hydroxide may be combined with the CeCC layer and/or be very thin, so that an area with oxygen as the main element was not detected on this alloy (Figure 3). A small section in which oxygen was the main element was only observed in the sample 2-Ce-5, but for a modest difference.

Signals in the transition zones between the three indicated sections (ascribed to CeCC, $\text{Al}_2\text{O}_3/\text{Al}(\text{OH})_3$, and Al matrix) underwent progressive changes due to the roughness of both the surface of the samples and the layers formed. Hence, the thickness of the coating and its sections could only be estimated. It should also be clarified that the initial erosion on the coating surface had very abrupt changes due again to the roughness of the sample. In this sense, it is common to estimate the thickness of each layer as the depth of erosion between the points where the signals of the main elements of each layer intersect the signals of the main element of adjacent layers [36,37]. In our case, the thicknesses were determined by the intersection between signals of Ce-O, Ce-Al, and O-Al. Hence, the thicknesses of the CeCC and alumina layers estimated according to this criterion from the GDOES profiles are presented in Table 4. A first result to be highlighted is the existence of a CeCC of ≈ 180 nm thickness in the sample 2-Ce-1, which could not be detected by SEM-EDX. A similar circumstance was described in the bibliography by De Nicoló et al. [36]. In general, a tendency to higher CeCC thicknesses was observed in both alloys as treatment time increased. Moreover, CeCC deposited on alloy 7075 was thicker than over alloy 2024 for the same times. Values ranged from 120 nm up to 850 nm for 2024 and between 260 nm and 950 nm for 7075. These results are in agreement with the interpretation of the SEM-EDX study, confirming a faster coating growth over alloy 7075. Volaric et al. [15] also found a faster formation of CeCC on alloy 7075 than on 2024 in similar experimental conditions to those employed here. The precipitation of Ce-bearing compounds is favored in alloys with a higher number of electrochemically active areas, especially IMPs, on which the cathodic reactions that produce the alkalization of the medium necessary for precipitation of Ce oxides and hydroxides take place (see Equations (1)–(4)). Thus, the possible reasons explaining why CeCC was deposited faster over the alloy 7075 are the highest density of IMPs and the presence of more electrochemically active IMPs in the alloy 7075. On one hand, alloy 7075 had higher content of alloy elements than 2024, as depicted in Table 1 (2024: Al 93.42 wt. %; 7075: Al 89.61 wt. %), which suggests that there may be a denser population of IMPs in the alloy 7075 compared to the alloy 2024. On the other hand, in general, it can be stated that coarse IMPs in AA7075 are mainly Fe-rich while in AA2024, there is S-phase ($\text{Al}(\text{Cu},\text{Mg})$) and Fe-rich IMPs [1]. Fe-rich IMPs usually display high cathodic potential difference with the matrix, in particular in AA7075 due to the high Mg and Zn content of the alloy. S-phase is very complex and can initially undergo selective dissolution of Mg and later behave as a cathodic intermetallic particle [38]. Other strengthening particles like MgZn_2 and θ -phase (Al_2Cu) are very small and most likely are less important in the deposition process of Ce species.

Table 4. Thickness of CeCC and alumina layer obtained from intersection of signals in GDOES depth profiles.

Treatment Time (Minutes)	CeCC (nm)		Al Oxide/Hydroxide (nm)	
	2024	7075	2024	7075
1	120	260	–	60
5	200	470	20	110
10	590	590	–	90
15	850	950	–	210

When Figure 3 is carefully analyzed, it can be noticed that the Ce signals in all profiles of alloy 2024 gradually dropped as the erosion depth increased. This descent got smoother as the deposition time increased. This fact can be interpreted as an increase in the homogeneity of the Ce content in the coating as the deposition time was prolonged, in addition to the already indicated increase in thickness. A similar trend is observed in Figure 4 for samples 7-Ce-1, 7-Ce-5, and 7-Ce-10. Subsequently, if the treatment time was increased up to 15 min, sample 7-Ce-15, the acquired Ce profile was different. The Ce signal firstly reached a maximum and then dropped similarly to the previous curves upon approaching the aluminum substrate. This shape can be justified on the basis of the high degree of surface cracking observed in the sample 7-Ce-15 by SEM.

Regarding the aluminum oxide/hydroxide thickness, it was almost stable close to 100 nm in samples 7-Ce-1, 7-Ce-5, and 7-Ce-10, and increased near to 200 nm in sample 7-Ce-15. On the 2024 alloy, only sample 2-Ce-5 showed a testimonial thickness of 20 nm.

3.3. Potentiodynamic Linear Polarization (LP)

Figure 5 shows the potentiodynamic linear polarization (LP) curves in 3.5% NaCl of samples prepared during different times of deposition. In addition, one representative sample without treatment, only subjected to acetone cleaning, was plotted for comparison.

All curves of coated samples in Figure 5 were placed at lower current densities than the corresponding bare alloys. Approximately, the corrosion current density (J_{corr}) of all coated samples was one order of magnitude lower than J_{corr} of the corresponding bare sample.

The corrosion potential (E_{corr}) of alloys 2024 and 7075 was -0.55 V and -0.66 V, respectively. It can be observed in Figure 5 that E_{corr} got more cathodic upon the deposition of CeCC for 1 min, samples 2-Ce-1 and 7-Ce-1. This trend was more intense in samples with 5, 10, and 15 min of treatment, E_{corr} 125–200 mV being more cathodic than those for uncoated alloys. In contrast, the pitting potential (E_{pit}) did not change significantly. As a consequence, a passive region appeared in all coated samples, with 100–200 mV width in samples 2-Ce and 15–125 mV width in samples 7-Ce. As a consequence, the susceptibility to pitting corrosion of the coated samples was reduced. Similar behavior was observed in [15], where E_{corr} shifted to more negative values and a passive region appeared. However, 2024 and 7075 samples required up to 1 h of conversion treatment in similar conditions than those reported here to reach a similar passive region ($|E_{\text{corr}} - E_{\text{pit}}| = 240$ mV for 2024, and $|E_{\text{corr}} - E_{\text{pit}}| = 190$ mV). When 10 min of conversion treatment was employed, a small shift of E_{corr} was found (30–40 mV).

Contrariwise, other authors did not observe a passive region. In [39], 2024-T3 and 7075-T7 alloys were employed to study the role of sodium hydroxide (alkaline cleaner) and nitric acid (desmutting) as pre-treatments prior to cerium treatment in $\text{Ce}(\text{NO}_3)_3$ at 85 °C with H_2O_2 . After CCCe treatments, the corrosion potentials shifted to more negative potentials, relative to those of the untreated alloys, by up to ~ 50 mV, except for the 7075-T6 alloy with a desmutting time of 30 s, for which the potential shift was ~ 300 mV. Indeed, a passive region was only detected for this last condition, while $E_{\text{pit}} = E_{\text{corr}}$ in the case of 2024 and other experimental condition tested for 7075.

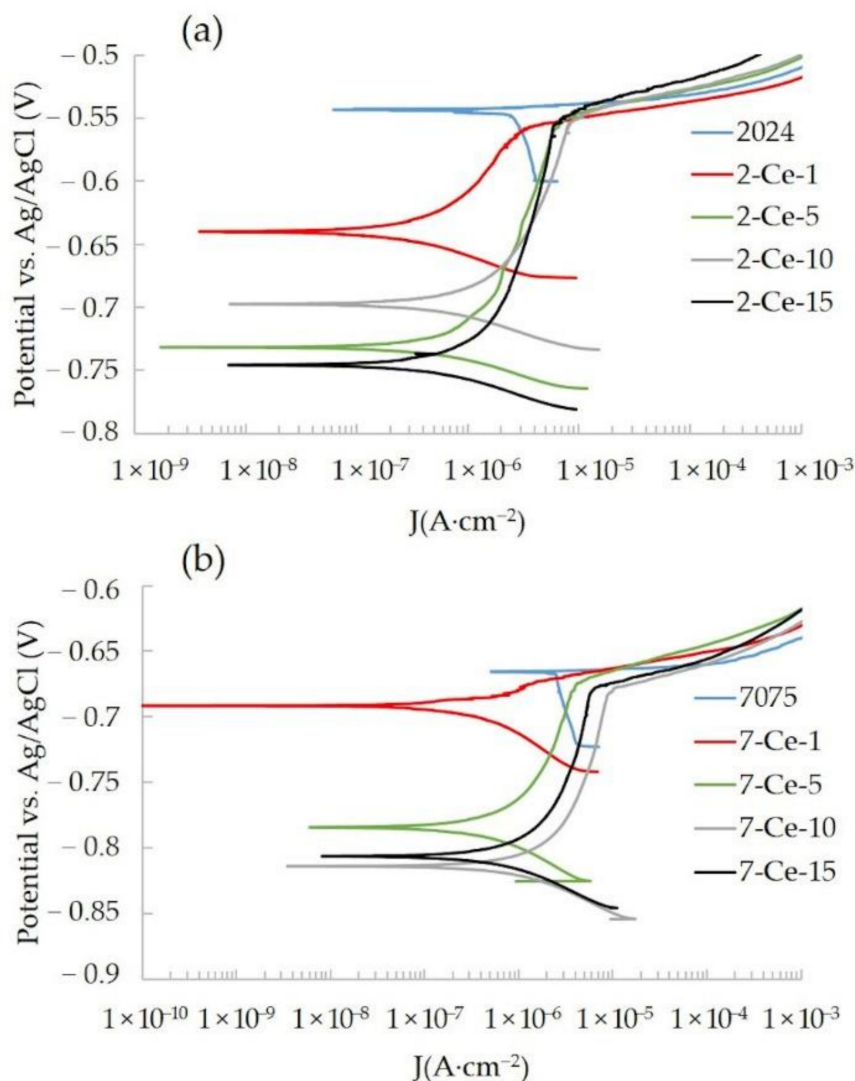


Figure 5. Potentiodynamic linear polarization (LP) curves in 3.5% NaCl. (a) 2024, (b) 7075.

According to the mixed potential theory, the simultaneous reduction of J_{corr} and E_{corr} observed when the CeCC was formed can be ascribed to a reduction in the cathodic reaction rate of the redox process. In turn, this reduction is related to a smaller number and area of cathodic sites exposed to the electrolyte [40]. In other words, a cathodic mechanism of protection was observed. This result is in agreement with others obtained in several aluminum alloys, including AA2017 [15,21,38,41].

3.4. Electrochemical Impedance Spectroscopy (EIS)

Nyquist diagrams of coated samples of alloys 2024 and 7075 are plotted in Figures 6 and 7, respectively. Meanwhile, the graph in Figure 8 contains the values of $|Z|$ at 0.01 Hz, denoted as $|Z|_{0.01}$, since the value of the impedance modulus at low frequency is usually considered representative of the corrosion resistance of the systems [42,43].

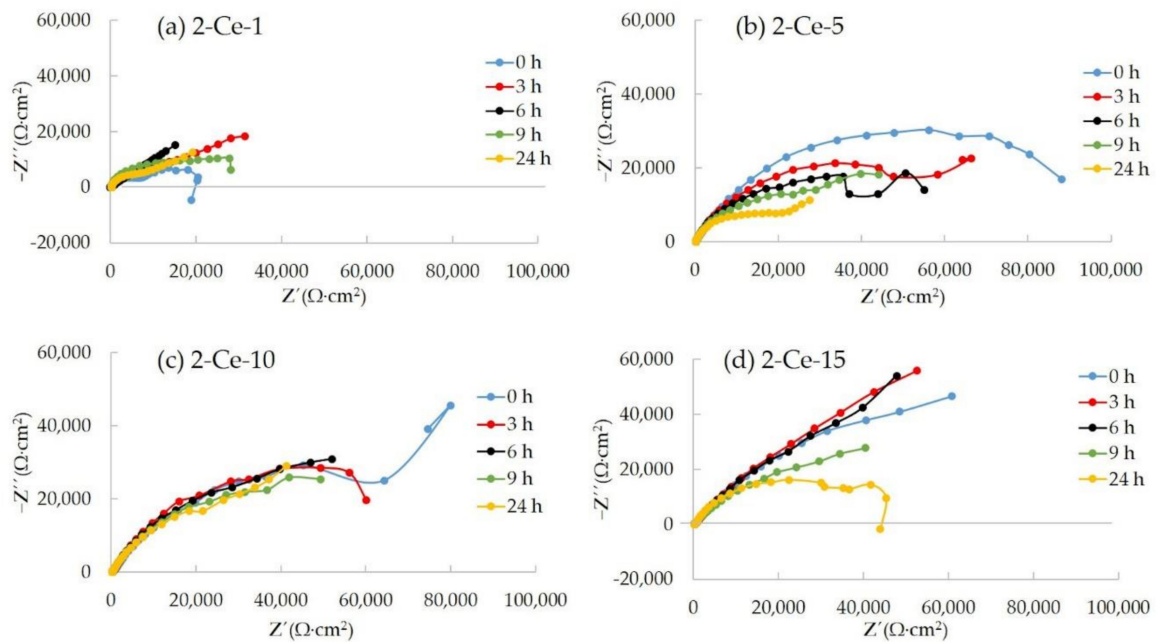


Figure 6. Nyquist diagrams during the immersion test in 0.5% NaCl of 2024 samples: (a) 2-Ce-1, (b) 2-Ce-5, (c) 2-Ce-10, and (d) 2-Ce-15.

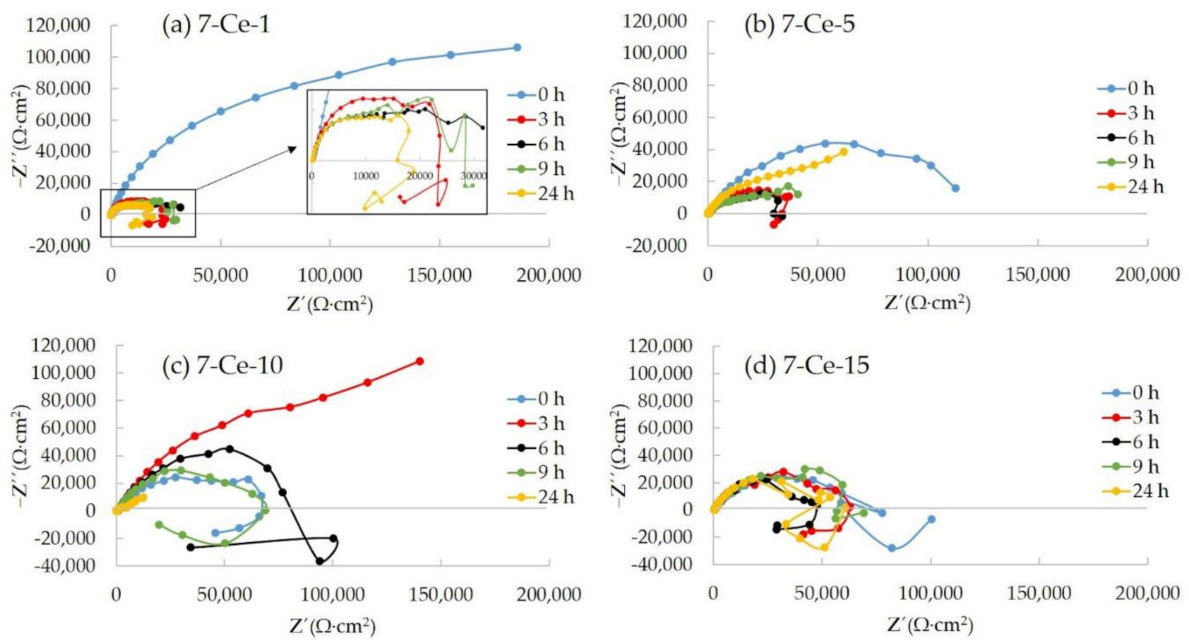


Figure 7. Nyquist diagrams during the immersion test in 0.5% NaCl of 7075 samples: (a) 7-Ce-1, (b) 7-Ce-5, (c) 7-Ce-10, and (d) 7-Ce-15.

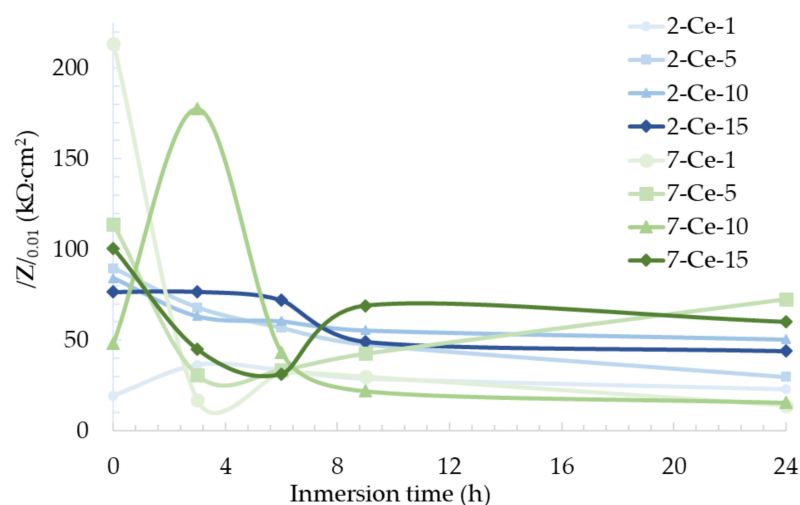


Figure 8. $/Z/_{0.01}$ during the immersion test in 0.5% NaCl.

Sample 2-Ce-1 showed an approximately stable behavior, with slight increases in both the size of arcs in Nyquist diagrams in Figure 6a and in $/Z/_{0.01}$ after 3 and 6 h of immersion and subsequent slight drops until the end of the test. $/Z/_{0.01}$ was $20 \text{ k}\Omega\cdot\text{cm}^2$ at the beginning and reached $34 \text{ k}\Omega\cdot\text{cm}^2$ after 6 h and $23 \text{ k}\Omega\cdot\text{cm}^2$ after 24 h. Incipient inductive loops could be observed at low frequencies in the Nyquist diagrams acquired at the beginning of the test and after 9 h. Various authors stated that this loop is related to the anodic behavior of the intermetallic phase Al(Cu, Mg) and the corresponding pitting nucleation and corrosion processes [44–46]. Thus, the existence of inductive loops could be due to IMPs not well protected because they were not completely coated during the formation of the CeCC or because this coating deteriorated over the course of the immersion test.

During the test of sample 2-Ce-5, Figure 6b, a continuous but moderate decrease of the impedance was evidenced, although there was no sign of inductive loops at low frequencies. $/Z/_{0.01}$ started at $90 \text{ k}\Omega\cdot\text{cm}^2$ and went to $30 \text{ k}\Omega\cdot\text{cm}^2$ after 24 h. Similarly, the Nyquist diagram of sample 2-Ce-10 in Figure 6c shows small changes and, accordingly, $/Z/_{0.01}$ was reduced from $84 \text{ k}\Omega\cdot\text{cm}^2$ to $51 \text{ k}\Omega\cdot\text{cm}^2$.

In the case of sample 2-Ce-15, Figure 6d, the impedance remained almost stable for 6 h of immersion. Afterwards, a decrease was found for 9 and 24 h. At the beginning, $/Z/_{0.01} = 77 \text{ k}\Omega\cdot\text{cm}^2$, after 6 h it was $/Z/_{0.01} = 72 \text{ k}\Omega\cdot\text{cm}^2$, and finally after 24 h $/Z/_{0.01} = 44 \text{ k}\Omega\cdot\text{cm}^2$.

Analyzing the EIS data of alloy 7075, sample 7-Ce-1 exhibited an important decline of the impedance in Figure 7a after only 3 h of immersion. $/Z/_{0.01}$ changed from $214 \text{ k}\Omega\cdot\text{cm}^2$ in the first minutes down to $17 \text{ k}\Omega\cdot\text{cm}^2$ 3 h later. At this time, an inductive loop at low frequencies appeared, indicating pitting corrosion phenomena. As already argued in the discussion of the EIS results of sample 2-Ce-1, this event was produced by pitting provoked due to the lack of perfect protection offered by the CeCC. Between 3 and 24 h, the inductive loop could be observed and the impedance decreased slightly both in the Nyquist diagram and the $/Z/_{0.01}$ value. Therefore, although 7-Ce-1 exhibited the highest $/Z/_{0.01}$ in the beginning of the immersion, Figure 8, this sample deteriorated remarkably.

The behavior of sample 7-Ce-5, Figure 7b, was similar to that of 7-Ce-1. The impedance after 3 h was lower than the impedance in the beginning. $/Z/_{0.01}$ suffered a reduction from $114 \text{ k}\Omega\cdot\text{cm}^2$ down to $31 \text{ k}\Omega\cdot\text{cm}^2$. Afterwards, the size of the arcs in the Nyquist diagram and their corresponding $/Z/_{0.01}$ remained almost constant after 6 and 9 h, with values of $34 \text{ k}\Omega\cdot\text{cm}^2$ and $43 \text{ k}\Omega\cdot\text{cm}^2$. There were also weak inductive loops at low frequencies in Nyquist diagrams after 3, 6, and 9 h. Once the sample was in the chloride solution for 24 h, a mild increase of the impedance was observed.

The Nyquist diagrams of the sample 7-Ce-10 are included in Figure 7c. It can be observed that the impedance increased after 3 h with respect to the diagram obtained

in the beginning. Later on, the impedance reduced with time. The diagram after 9 h was very similar to the one acquired in the beginning and clearly lower after 24 h. The values of $|Z|_{0.01}$ reflect the same trend. $|Z|_{0.01} = 49 \text{ k}\Omega\cdot\text{cm}^2$ in the beginning. It scaled to $178 \text{ k}\Omega\cdot\text{cm}^2$ after 3 h and went down to $43 \text{ k}\Omega\cdot\text{cm}^2$, $22 \text{ k}\Omega\cdot\text{cm}^2$, and $16 \text{ k}\Omega\cdot\text{cm}^2$ after 6, 9, and 24 h. In addition, inductive loops at low frequencies could be found in the diagrams registered in the beginning and after 6 and 9 h.

Finally, sample 7-Ce-15 in Figure 7d showed a stable behavior during the immersion without signs of reduction in the impedance. $|Z|_{0.01}$ values were around $50 \text{ k}\Omega\cdot\text{cm}^2$. However, there were inductive loops at low frequencies in the diagrams obtained at all times studied.

As a whole, the EIS results of all the samples showed similar impedance after 24 h of immersion in the 0.1% NaCl solution, with $|Z|_{0.01}$ in the range $15\text{--}70 \text{ k}\Omega\cdot\text{cm}^2$. There were inductive loops at low frequencies in samples of both alloy 2024 and 7075, indicating pitting corrosion. However, these loops were more common and well defined in the 7075 samples than in 2024. Moderate increases of the impedance and disappearance of inductive loops may be related to temporary protective effects of corrosion products or to a certain self-healing activity of the Ce coatings [12,14].

3.5. Neutral Salt Spray (NSS) Test

Based on the above results, it was decided to perform NSS test on samples deposited for 10 min: 2-Ce-10 and 7-Ce-10. The criteria for selecting this time were numerous. First, SEM images showed a general coverage of the surface for samples treated for 10 min or more (2-Ce-10, 2-Ce-15, 7-Ce-10, 7-Ce-15), without bare areas. Second, all coated samples had comparable J_{corr} ($\approx 10^{-6} \text{ A/cm}^2$). Third, samples for 10 and 15 min of deposition exhibited similar degradations in the EIS study. Thus, with similar performances, the sample that required the shortest preparation time was chosen.

Images of samples 2/7-Ce-10 after 72 and 96 h of NSS test are shown in Figure 9. For comparison purposes, images of bare alloys 2024 and 7075 after 96 h are also included in Figure 9. White corrosion products can be observed in all the images, although to different extents depending on the sample. Samples 2/7-Ce-10 had corrosion products in some areas after 72 h, Figure 9a,b. The area covered by corrosion products was higher after 96 h, Figure 9c,d, than after 72 h. Sample 2-Ce-10, image 9c, exhibited a lower degree of corrosion attacks than 7-Ce-10, image 9d. Finally, the samples showing the highest coverage of white corrosion products were bare samples after 96 h of NSS test, Figure 9e,f. The reduced deterioration in samples with CeCC deposition corroborates the protective behavior of the CeCC.

By comparing corrosion resistance results (electrochemical and NSS test) with the coating thicknesses estimated by GDOES, we can conclude that there is no direct relationship between them. That is, without ruling out the effect of thickness, corrosion resistance should depend primarily on other factors, such as the presence of coating on the places where corrosion processes take place and the compactness of the CeCC, provided that a more compact layer will prevent chloride ions from accessing the metal more effectively than a cracked layer.

Although better results in NSS test than those obtained here are claimed in the literature for CeCC [14,47,48], it should be considered that CeCC usually shows poor or variable NSS performance in the unsealed condition, which was the case here tested. Moreover, the reported studies usually suffer from various drawbacks [14], such as different performance depending on the alloy treated, reproducibility issues, or small and non-standard panels tested. Therefore, some future works of the research reported here could be the implementation of suitable sealing post-treatments and the study of reproducibility in NSS tests of various aluminum alloys.

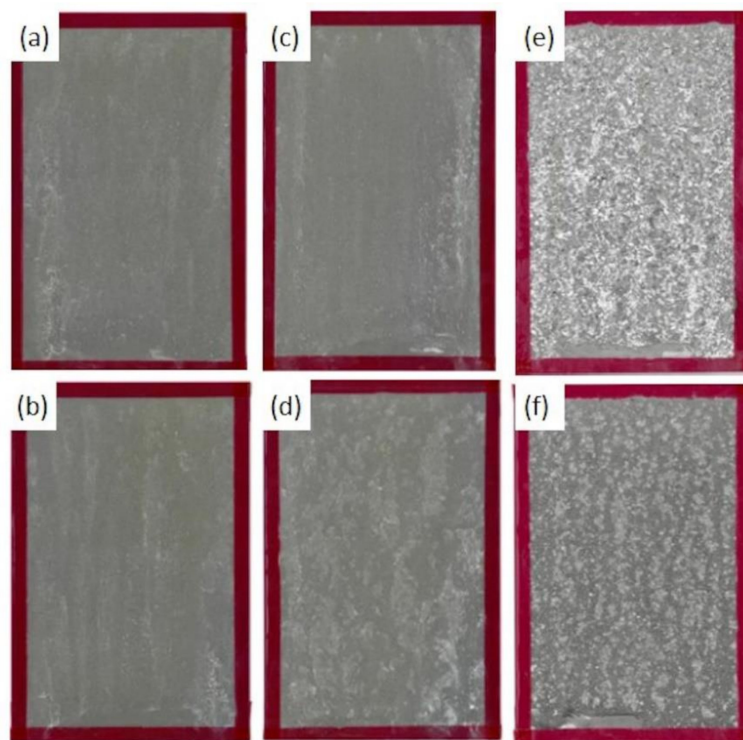


Figure 9. Samples after 72 h of NSS test: (a) 2-Ce-10 and (b) 7-Ce-10. Samples after 96 h of SST: (c) 2-Ce-10, (d) 7-Ce-10, (e) 2024-bare, and (f) 7075-bare.

4. Conclusions

In this work, new steps were taken in the implementation of CeCC as alternatives to CrCC, showing that commercial surface pretreatments used in the aeronautical industry allow CeCC to be deposited in aluminum alloys 2024 and 7075. The CeCC proved to be protective in NaCl solutions and in the NSS test. Notably, the CeCC formed in standard test samples of 100 mm × 150 mm provided corrosion protection in NSS test, which is the reference corrosion test in the aeronautical industry.

SEM-EDX results indicated that the cerium layer was firstly observed as deposits grown over the intermetallic phases. As the deposition proceeded, a more widespread covering of the surface was observed and a tendency to the formation of cracks was seen where the coating was thicker. When comparing between alloys, both the deposits and cracked coating appeared at shorter times of deposition in alloy 7075.

GDOES results showed that the thickness of the cerium layer increased over time of deposition and that the layers grew faster on alloy 7075 than on 2024, obtaining thicker coatings on 7075 employing identical experimental conditions. GDOES also unveiled that there was a Ce-rich layer in both alloys, and that there was also an aluminum oxide/hydroxide layer on alloy 7075 between the upper Ce-rich layer and the aluminum matrix.

CeCC coating was observed to offer cathodic protection in 3.5% NaCl solutions in both alloys. Corrosion resistance estimated by electrochemical techniques (linear polarization and electrochemical impedance spectroscopy) was of the same order of magnitude in all samples with CeCC. Likewise, CeCC provided corrosion protection in the NSS test. These results show that the thickness of CeCC was not the parameter ruling the corrosion resistance, which should be governed by other factors, such as the presence of coating on the places where corrosion processes take place and the compactness of the CeCC.

Future steps to follow in this line of research should focus on optimizing the experimental deposition parameters of the cerium layer and/or the use of posttreatments, in order to further enhance the corrosion resistance of the CeCC.

Supplementary Materials: The following are available online at <https://www.mdpi.com/article/10.3390/met11060930/s1>, Figure S1: EDX spectra in areas marked in Figure 1, Figure S2: EDX spectra in areas marked in Figure 2.

Author Contributions: Conceptualization, L.G.-R., M.B., F.J.B. and L.F.; methodology, L.G.-R., M.B., J.J.A.-G. and L.F.; formal analysis, L.G.-R., M.B. and J.J.A.-G.; investigation, J.J.A.-G., M.L. and F.A.; resources, F.J.B. and L.F.; writing—original draft preparation, J.J.A.-G. and L.G.-R.; writing—review and editing, M.B. and F.A. All authors have read and agreed to the published version of the manuscript.

Funding: This research was funded by the Ministry of Economy, Industry and Competitiveness of Spain/FEDER Program of the EU. Project: Optimización y viabilidad industrial del proceso de preparación de capas de conversión basadas en cerio sobre aleaciones de aluminio. Reference MAT2014-60857-R. The APC was funded by Instituto Universitario de Investigación Marina (INMAR) of the University of Cádiz and the Programa de Fomento e Impulso de la Actividad de Investigación y Transferencia of the University of Cádiz.

Data Availability Statement: The data presented in this study are available on request from the corresponding author.

Acknowledgments: The authors acknowledge Alex Lanzuti (University of Udine) for the GDOES measurements and help in the interpretation of results. The authors would also like to acknowledge Titania, Ensayos y Proyectos Industriales S.L. for the support in the achievements of this work. L.G.R. acknowledges support from the Programme for Attracting Talent of UCA (Vice-rectorate for Technology Transfer and Innovation). J.J.A.G. acknowledges the Vice-rectorate for Research of UCA (Contratos predoctorales PIF, Plan Propio 2015).

Conflicts of Interest: The authors declare no conflict of interest.

References

1. Parvizi, R.; Tan, M.Y.; Hughes, A.E. Chapter 14. Recent Insights in to Corrosion Initiation at the Nanoscale. In *Fundamentals of Aluminium Metallurgy*; Lumley, R.N., Ed.; Woodhead Publishing, Elsevier: Cambridge, UK, 2018; pp. 525–551.
2. Zhu, Y.; Sun, K.; Frankel, G.S. Intermetallic Phases in Aluminum Alloys and Their Roles in Localized Corrosion. *J. Electrochem. Soc.* **2018**, *165*, C807–C820. [[CrossRef](#)]
3. Hughes, A.E.; Parvizi, R.; Forsyth, M. Microstructure and corrosion of AA2024. *Corros. Rev.* **2015**, *33*, 1–30. [[CrossRef](#)]
4. Kendig, M.; Jeanjaquet, S.; Addison, R.; Waldrop, J. Role of hexavalent chromium in the inhibition of corrosion of aluminum alloys. *Surf. Coat. Technol.* **2001**, *140*, 58–66. [[CrossRef](#)]
5. Hughes, E. Conversion coatings. In *Encyclopedia of Interfacial Chemistry: Surface Science and Electrochemistry*; Wandelt, K., Ed.; Elsevier: Amsterdam, The Netherlands, 2018; pp. 108–114. [[CrossRef](#)]
6. Ferreira, G.S.; Zheludkevich, M.L.; Tedim, J.; Yasakau, K.A. 9-Self-healing nanocoatings for corrosion control. In *Corrosion Protection and Control Using Nanomaterials*; Saji, V.S., Cook, R., Eds.; Woodhead Publishing Series in Metals and Surface Engineering: Cambridge, UK, 2012; pp. 213–263. [[CrossRef](#)]
7. Zarras, P.; Stenger-Smith, J.D. Chapter 3. Smart inorganic and organic pretreatment coatings for the inhibition of corrosion on metals/alloys. In *Intelligent Coatings for Corrosion Control*; Tiwari, A., Rawlins, J., Hihara, L.H., Eds.; Butterworth-Heinemannpp: London, UK, 2014; pp. 59–91. [[CrossRef](#)]
8. Kwakernaak, A.; Hofstede, J.; Poulis, J.; Benedictus, R. Improvements in bonding metals for aerospace and other application. In *Welding and Joining of Aerospace Materials*; Chaturvedi, M.C., Ed.; Woodhead Publishing Series in Welding and Other Joining Technologies: Cambridge, UK, 2012; pp. 235–287. [[CrossRef](#)]
9. Eichinger, E.; Osborne, J.; Van Cleave, T. Hexavalent chromium elimination: An aerospace industry progress report. *Met. Finish.* **1997**, *95*, 36–41. [[CrossRef](#)]
10. Qi, J.; Gao, L.; Li, Y.; Wang, Z.; Thompson, G.E.; Skeldon, P. An Optimized Trivalent Chromium Conversion Coating Process for AA2024-T351 Alloy. *J. Electrochem. Soc.* **2017**, *164*, C390–C395. [[CrossRef](#)]
11. Kendig, M.W.; Buchheit, R.G. Corrosion Inhibition of Aluminum and Aluminum Alloys by Soluble Chromates, Chromate Coatings, and Chromate-Free Coatings. *Corrosion* **2003**, *59*, 379–400. [[CrossRef](#)]
12. Becker, M. Chromate-free chemical conversion coatings for aluminum alloys. *Corros. Rev.* **2019**, *37*, 321–342. [[CrossRef](#)]
13. Stoica, A.-I.; Światowska, J.; Romaine, A.; Di Franco, F.; Qi, J.; Mercier, D.; Seyeux, A.; Zanna, S.; Marcus, P. Influence of post-treatment time of trivalent chromium protection coating on aluminium alloy 2024-T3 on improved corrosion resistance. *Surf. Coat. Technol.* **2019**, *369*, 186–197. [[CrossRef](#)]
14. Harvey, T.G. Cerium-based conversion coatings on aluminium alloys: A process review. *Corros. Eng. Sci. Technol.* **2013**, *48*, 248–269. [[CrossRef](#)]

15. Volarič, B.; Mazare, A.; Virtanen, S.; Milošev, I. The Effect of Deposition Parameters on the Properties of CeCl₃ and LaCl₃ Conversion Coatings Deposited on Three Al-Based Substrates. *Corrosion* **2019**, *76*, 18–38. [CrossRef]
16. Milošev, I.; Frankel, G.S. Review—Conversion Coatings Based on Zirconium and/or Titanium. *J. Electrochem. Soc.* **2018**, *165*, C127–C144. [CrossRef]
17. Klumpp, R.E.; Donatus, U.; Da Silva, R.M.P.; Antunes, R.A.; Machado, C.D.S.C.; Milagre, M.X.; Araujo, J.V.D.S.; De Viveiros, B.V.G.; Costa, I. Corrosion protection of the AA2198-T8 alloy by environmentally friendly organic-inorganic sol-gel coating based on bis-1,2-(triethoxysilyl) ethane. *Surf. Interface Anal.* **2021**, *53*, 314–329. [CrossRef]
18. Bouali, A.; Serdechnova, M.; Blawert, C.; Tedim, J.; Ferreira, M.; Zheludkevich, M. Layered double hydroxides (LDHs) as functional materials for the corrosion protection of aluminum alloys: A review. *Appl. Mater. Today* **2020**, *21*, 100857. [CrossRef]
19. Milošev, I. Contemporary Modes of Corrosion Protection and Functionalization of Materials. *Acta Chim. Slov.* **2019**, *66*, 511–533. [CrossRef]
20. Bethencourt, M.; Botana, F.; Calvino, J.J.; Marcos, M.; Rodríguez-Chacón, M. Lanthanide compounds as environmentally-friendly corrosion inhibitors of aluminium alloys: A review. *Corros. Sci.* **1998**, *40*, 1803–1819. [CrossRef]
21. Sainis, S.; Roşoiu, S.; Ghassemali, E.; Zanella, C. The role of microstructure and cathodic intermetallics in localised deposition mechanism of conversion compounds on Al (Si, Fe, Cu) alloy. *Surf. Coat. Technol.* **2020**, *402*, 126502. [CrossRef]
22. Czerwinski, F. Cerium in aluminum alloys. *J. Mater. Sci.* **2020**, *55*, 24–72. [CrossRef]
23. Decroly, A.; Petitjean, J.-P. Study of the deposition of cerium oxide by conversion on to aluminium alloys. *Surf. Coat. Technol.* **2005**, *194*, 1–9. [CrossRef]
24. Scholes, F.; Soste, C.; Hughes, A.; Hardin, S.; Curtis, P. The role of hydrogen peroxide in the deposition of cerium-based conversion coatings. *Appl. Surf. Sci.* **2006**, *253*, 1770–1780. [CrossRef]
25. Amaya, J.M.S.; Blanco, G.; Garcia-Garcia, F.J.; Bethencourt, M.; Botana, F. XPS and AES analyses of cerium conversion coatings generated on AA5083 by thermal activation. *Surf. Coat. Technol.* **2012**, *213*, 105–116. [CrossRef]
26. Hughes, A.; Harvey, T.; Biribilis, N.; Kumar, A.; Buchheit, R. Coatings for corrosion prevention based on rare earths. In *Rare Earth-Based Corrosion Inhibitors*; Elsevier: Amsterdam, The Netherlands, 2014; pp. 186–232.
27. Klumpp, R.E.; Donatus, U.; Araujo, J.V.S.; Redigolo, M.; Machado, C.D.S.C.; Costa, I. The Effect of Acid Pickling on the Corrosion Behavior of a Cerium Conversion-Coated AA2198-T851 Al-Cu-Li Alloy. *J. Mater. Eng. Perform.* **2020**, *29*, 167–174. [CrossRef]
28. Andreeva, R. On the Role of pre-treatment of Aluminum Substrate on Deposition of Cerium Based Conversion Layers and Their Corrosion-Protective Ability. *Int. J. Electrochem. Sci.* **2018**, *13*, 5333–5351. [CrossRef]
29. Alba-Galvín, J.J.; González-Rovira, L.; Bethencourt, M.; Botana, F.J.; Sánchez-Amaya, J.M. Influence of Aerospace Standard Surface Pretreatment on the Intermetallic Phases and CeCC of 2024-T3 Al-Cu Alloy. *Metals* **2019**, *9*, 320. [CrossRef]
30. ISO 9227:2017. Corrosion Tests in Artificial Atmospheres—Salt Spray Tests. Available online: <https://www.iso.org/standard/63543.html> (accessed on 29 April 2019).
31. ASTM B117-18. Standards Practice for Operating Salt Spray (Fog) Apparatus. Available online: <https://www.astm.org/Standards/B117> (accessed on 29 April 2019).
32. Lau, D.; Glenn, A.; Hughes, A.; Scholes, F.; Muster, T.; Hardin, S. Factors influencing the deposition of Ce-based conversion coatings, Part II: The role of localised reactions. *Surf. Coat. Technol.* **2009**, *203*, 2937–2945. [CrossRef]
33. Rodič, P.; Milošev, I. Corrosion resistance of cerium-conversion coatings formed from cerium(III) salts on aluminium alloy 7075-T6. *Studia Univ. Babeş-Bolyai Chem.* **2020**, *65*, 227–244. [CrossRef]
34. Shimizu, K.; Brown, G.; Habazaki, H.; Kobayashi, K.; Skeldon, P.; Thompson, G.; Wood, G. Impurity distributions in barrier anodic films on aluminium: A GDOES depth profiling study. *Electrochim. Acta* **1999**, *44*, 2297–2306. [CrossRef]
35. Kuypers, S.; Buytaert, G.; Terryn, H. Depth profiling of rolled aluminium alloys by means of GDOES. *Surf. Interface Anal.* **2004**, *36*, 833–836. [CrossRef]
36. De Nicolò, A.; Paussa, L.; Gobessi, A.; Lanzutti, A.; Cepek, C.; Andreatta, F.; Fedrizzi, L. Cerium conversion coating and sol-gel multilayer system for corrosion protection of AA6060. *Surf. Coat. Technol.* **2016**, *287*, 33–43. [CrossRef]
37. Andreatta, F.; Lanzutti, A.; Paussa, L.; Fedrizzi, L. Addition of phosphates or copper nitrate in a fluotitanate conversion coating containing a silane coupling agent for aluminium alloy AA6014. *Prog. Org. Coat.* **2014**, *77*, 2107–2115. [CrossRef]
38. Bethencourt, M.; Botana, F.J.; Cano, M.J.; González-Rovira, L.; Marcos, M.; Amaya, J.M.S. Protection by Thermal and Chemical Activation with Cerium Salts of the Alloy AA2017 in Aqueous Solutions of NaCl. *Met. Mater. Trans. A* **2011**, *43*, 182–194. [CrossRef]
39. De Frutos, A.; Arenas, M.A.; Liu, Y.; Skeldon, P.; Thompson, G.; De Damborenea, J.; Conde, A. Influence of pre-treatments in cerium conversion treatment of AA2024-T3 and 7075-T6 alloys. *Surf. Coat. Technol.* **2008**, *202*, 3797–3807. [CrossRef]
40. García-Rubio, M.; Ocón, P.; Climent-Font, A.; Smith, R.; Curioni, M.; Thompson, G.; Skeldon, P.; Lavia, A.; Garcia, I. Influence of molybdate species on the tartaric acid/sulphuric acid anodic films grown on AA2024 T3 aerospace alloy. *Corros. Sci.* **2009**, *51*, 2034–2042. [CrossRef]
41. Hu, J.; Zhao, X.; Tang, S.; Ren, W.; Zhang, Z. Corrosion resistance of cerium-based conversion coatings on alumina borate whisker reinforced AA6061 composite. *Appl. Surf. Sci.* **2007**, *253*, 8879–8884. [CrossRef]
42. Feliu, J.S. Electrochemical Impedance Spectroscopy for the Measurement of the Corrosion Rate of Magnesium Alloys: Brief Review and Challenges. *Metals* **2020**, *10*, 775. [CrossRef]
43. Zheludkevich, M.; Yasakau, K.; Bastos, A.; Karavai, O.; Ferreira, M. On the application of electrochemical impedance spectroscopy to study the self-healing properties of protective coatings. *Electrochem. Commun.* **2007**, *9*, 2622–2628. [CrossRef]

44. Bethencourt, M.; Botana, F.; Cano, M.; Marcos, M.; Amaya, J.M.S.; Rovira, L.G. Behaviour of the alloy AA2017 in aqueous solutions of NaCl. Part I: Corrosion mechanisms. *Corros. Sci.* **2009**, *51*, 518–524. [[CrossRef](#)]
45. Ilevbare, G.O.; Scully, J.R.; Yuan, J.; Kelly, R.G. Inhibition of Pitting Corrosion on Aluminum Alloy 2024-T3: Effect of Soluble Chromate Additions vs Chromate Conversion Coating. *Corrosion* **2000**, *56*, 227–242. [[CrossRef](#)]
46. Aballe, A.; Bethencourt, M.; Botana, F.J.; Marcos, M.; Rodríguez-Chacón, M.A. Seguimiento de la corrosión de la aleación AA2024 en disoluciones de NaCl mediante la medida del ruido electroquímico. *Rev. Met.* **1998**, *34*, 42–46. [[CrossRef](#)]
47. Fahrenholtz, W.G.; O’Keefe, M.J.; Zhou, H.; Grant, J. Characterization of cerium-based conversion coatings for corrosion protection of aluminum alloys. *Surf. Coat. Technol.* **2002**, *155*, 208–213. [[CrossRef](#)]
48. Rivera, B.F.; Johnson, B.Y.; O’Keefe, M.J.; Fahrenholtz, W. Deposition and characterization of cerium oxide conversion coatings on aluminum alloy 7075-T6. *Surf. Coat. Technol.* **2004**, *176*, 349–356. [[CrossRef](#)]